

EFFECTS OF DEFECTS ON INTERLAMINAR PERFORMANCE OF COMPOSITES

Andrew Makeev*, Yuri Nikishkov, Guillaume Seon, and Erian Armanios
Department of Mechanical and Aerospace Engineering
University of Texas at Arlington, Arlington, Texas, U.S.A.

Abstract

This work presents a methodology for accurate assessment of the effects of manufacturing defects on the interlaminar tensile (ILT) strength and fatigue performance of composites used in rotorcraft fatigue-critical structural designs. A primary failure mechanism for such structures is delamination. Although the ILT strength and fatigue material properties are essential for the development of the analysis methods able to predict the onset of delamination, there are no reliable methods to determine such properties. A major technical challenge is extreme sensitivity of the ILT behavior to manufacturing defects including porosity that could lead to unacceptable scatter in the test results. In this work, X-Ray Computed Tomography (CT) measurements of porosity defects present in curved-beam test articles are integrated into finite element based stress analysis to capture the effects of defects on the ILT strength and fatigue behavior. Once the effects of manufacturing defects are captured through transfer of the CT measurements into a three-dimensional finite element model, the contribution of the defects to scatter in the test data could be quantified, and reliable interlaminar material properties determined. The ability to extract accurate ILT material properties from curved-beam tests is verified through an alternative test method developed to determine ILT strength for a pristine material structure. Such defect-free material strength provides a rigorous basis for assessing effects of defects.

1. INTRODUCTION¹

Currently, composite structural designs adopt metal design philosophy and use the same factor of safety of 1.5 to determine the ultimate design load from the limit load even though composite parts are inherently more susceptible to variations in manufacturing processes than metal parts. In addition to material variation in the resin content, bulk factor, and fiber alignment, part fabrication process variations such as operator skill, tooling setup, humidity fluctuation, equipment control, etc. are common causes that contribute to variation in part quality. Consequently, the increased sensitivity of composite part quality to material and process variations lowers production yields. In order to increase production yields, heavy burden is placed on composite manufacturing communities to understand and control their processes. Production yields of greater than 90% remain a "hit-and-miss" target [1].

The effects of manufacturing process parameters on structural strength and durability are not well understood. In particular, effects of inadequate design method and manufacturing process used to produce carbon/epoxy and glass/epoxy composite aircraft fatigue-critical, flight-critical components manifest themselves as defects such as porosity/voids, and

such defects impact the residual capability and the useful life of these components.

Manufacturing defects can severely deteriorate the matrix-dominated properties of composites, resulting in degraded strength and fatigue structural performance. Although it might not be practical to eliminate all the defects in a composite part, it is possible to avoid assumptions of the worst-case scenario and address improved part durability and damage tolerance once the defects and their effects are captured. Advanced structural methods that account for manufacturing defects in composite parts are needed to enable accurate assessment of their capability and useful life and enhance current design and maintenance practices.

One of the major barriers to accurately predict failure for polymer-matrix composites has been the lack of reliable matrix-dominated material properties which could be used as a basis for the development of accurate failure criteria [2, 3]. In particular, the interlaminar tensile (ILT) strength and fatigue properties which are generally the weakest basic material characteristics of a laminated composite system have been challenging to characterize. Accurate measurements of ILT strength and fatigue performance characteristics are needed to capture delamination failure which is one of the primary failure modes for rotorcraft composite structural designs. Glass-fiber and carbon-fiber reinforced epoxy-matrix prepreg composites, susceptible to delamination, are

¹ Presented at the 39th European Rotorcraft Forum, Moscow, Russia, September 3-6, 2013.

* Corresponding author, e-mail: makeev@uta.edu.

most commonly used in the design of rotorcraft composite structures.

Helicopter rotor systems are subject to extreme fatigue environments. Fatigue capability is a limiting factor for high-cycle components found in the helicopter dynamic systems [4]. Typical examples of the fatigue-critical primary composite structures include main rotor blade spars and yokes in commercial and military helicopters [5]. The primary failure mechanism for such structures is delamination. Accurate ILT and interlaminar shear (ILS) fatigue material properties integrated in reliable failure criteria are essential for the development of the analysis methods able to capture fatigue delamination. In particular, Reference [3] successfully used ILT and ILS *S-N* fatigue curves in the formulation of stress-based and fracture-based fatigue failure criteria to predict the onset and propagation of matrix-dominated failure modes including delaminations. However, the development of failure prediction methods is currently limited by the lack of reliable ILT material properties.

A major technical challenge to characterizing ILT behavior is extreme sensitivity to manufacturing defects including porosity that could lead to unacceptable scatter in the test results. Composite components of helicopter rotor systems are typically thick and oftentimes have areas with tight radius of curvature [4], which make them especially prone to porosity defects. Rotorcraft industry has been extensively making test articles representative of curved structural details of composite parts to better understand the effects of porosity. However, there is no consensus on the accept/reject criteria for assessing the effects of porosity on strength and fatigue performance. It has been determined that porosity volume content is not a reliable basis for capturing the effects of defects.

A relatively simple test specimen that could become a standard across the industry for characterizing porosity in composite structures, and the analysis methodology able to determine the key elements for capturing of the effects of defects on structural performance would be extremely beneficial.

To the best of the authors' knowledge, there are no standard test methods for assessment of ILT fatigue performance of composites. However, there are two American Society for Testing and Materials (ASTM) standard methods for measuring ILT strength.

Currently, ASTM D 6415 curved-beam (CB) test is a standard practice for measuring the ILT strength [6]. Figure 1 shows a typical CB test setup for a 0.26-inch thick unidirectional carbon/epoxy tape system. The failure mode is tensile delamination that starts in the radius area, typically at about two third of the thickness corresponding to the maximum interlaminar tensile stress location, and quickly propagates through

the flanges. The ASTM D 6415 provides a closed-form approximation of the ILT strength [6 – 8].

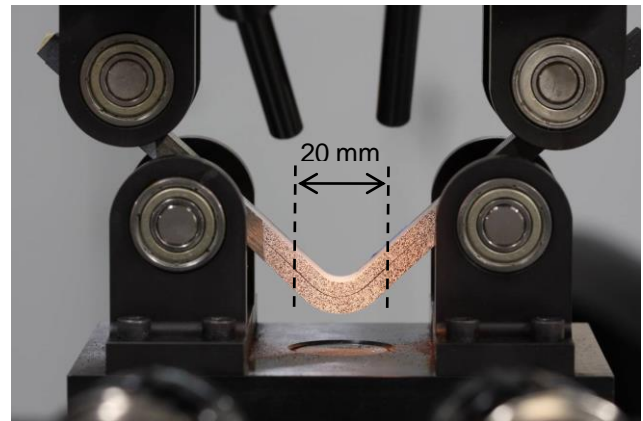


Figure 1. ASTM D 6415 test setup and tensile delamination failure of a unidirectional IM7/8552 carbon/epoxy CB specimen. Dashed lines indicate the area subject to CT scanning.

The authors measured ASTM D 6415 CB strength for multiple unidirectional carbon-fiber and glass-fiber reinforced epoxy-matrix prepreg tape composites. Based on their experience, the curved-beam strength data typically exhibit large scatter. For example, for 0.26-inch thick CB coupons manufactured from Hexcel IM7/8552 unidirectional tape [9] and cured per manufacturer's specifications, the average ASTM D 6415 interlaminar tensile strength value varies between 68.9 MPa (10 Ksi) and 82.7 MPa (12 Ksi) with a coefficient of variation (COV) usually higher than 20%. This raises doubts concerning the adequacy of the ASTM D 6415 standard as a coupon-independent test for measuring true ILT material strength. Large scatter in the material characterization test results may reflect the manufacturing quality as much as the materials properties.

Another method for assessing the ILT strength is ASTM D 7291 which applies a tensile force normal to the plane of a composite laminate using adhesively bonded thick metal end-tabs [10]. As noted in Ref [10], through-the-thickness strength results generated using this method will not, in general, be comparable to ASTM D 6415 since ASTM D 7291 subjects a relatively large volume of material to a quasi-uniform stress field while ASTM D 6415 subjects a small volume of material to a non-uniform stress field. Moreover, characterizing ILT strength using ASTM D 7291 is perhaps more challenging than ASTM D 6415 as failure could occur in the bond lines between the composite and the metal end-tabs.

The objective of this work is to develop efficient and accurate methods to capture the effects of porosity on the ILT strength and fatigue material behavior. Once the effects of manufacturing defects are understood, the contribution of the defects to scatter in the test

data could be quantified, and reliable material properties extracted.

ADTM D 6415 CB specimens are well suited for assessing the effects of porosity on ILT strength and fatigue performance. Porosity can be easily introduced in the CB specimens; the CB radius area susceptible to delamination onset is far away from the attachments of the test fixture; and the nondestructive inspections can be limited to the radius area. Therefore, such specimens could arguably be the strongest candidate to assess the effects of porosity on ILT strength and fatigue behavior.

The ability to extract accurate ILT material properties from CB tests must be verified. To this end, the recently developed short-beam (SB) method [11] is expanded to enable measurement of the ILT strength for pristine material structure; and establish a rigorous basis for assessing the effects of manufacturing defects in the CB specimens.

2. SHORT-BEAM METHOD

Short-beam (SB) specimens are prismatic coupons with uniform rectangular cross-sections and subject to three-point bending. Reference [11] provides the details of the methodology for assessing multiple stress-strain constitutive relations, based on the SB tests and the digital image correlation (DIC) technique-based deformation measurement. The dimensions of the SB coupons and the test fixture attachments were modified compared to ASTM D 2344 [12] in order to generate accurate stress-strain curves as well as consistent failure modes [11, 13]. SB test coupons have been machined in the zero-degree and 90-degree directions from unidirectional tape panels and loaded in the 1-2 (in-ply), 1-3 (interlaminar) and 2-3 principal material planes to characterize the shear stress-strain relations; Young's moduli in the zero-degree and 90-degree directions; and the Poisson's ratios. The fiber direction is denoted as 1 (zero-degree); the in-ply transverse direction as 2 (90-degree); and the laminate thickness direction as 3 (interlaminar direction.)

To characterize ILT material properties in this work, six SB specimens were machined in the thickness direction from a 106-ply thick IM7/8552 carbon/epoxy unidirectional tape panel cured at 350°F per prepreg manufacturer's specifications [9]. The cured ply-thickness was approximately 0.183 mm (0.0072 in) resulting in 19.4-mm (0.76-in) panel thickness. The SB specimen length was 19.4-mm (0.76-in). The coupons were 3.8-mm (0.15-in) thick, and 2.8-mm (0.11-in) wide. The coupon thickness corresponds to the in-ply 90-degree principal material direction; and the 2-3 principal material plane is the plane of loading. Figure 2 shows a schematic of a SB coupon and the loading conditions.

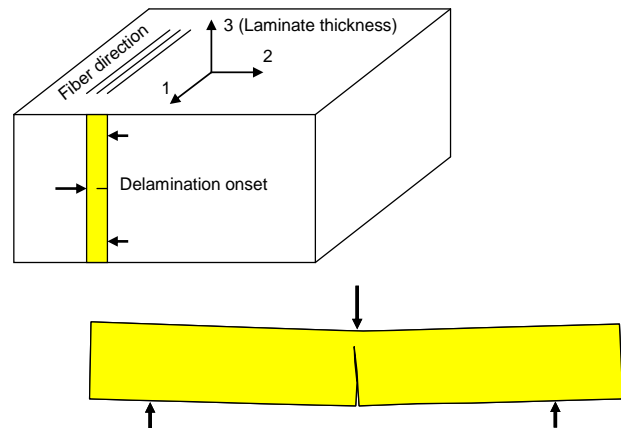


Figure 2. A SB coupon machined from a thick plate in the interlaminar (thickness) direction; loading conditions; and the interlaminar tensile failure.

To assess the ILT strength, the SB specimens were placed in an ASTM D 2344 test fixture with a 0.5-inch diameter loading nose and 0.125-inch diameter supports; and loaded in an electromechanical load frame at a constant 0.05 in/min crosshead displacement rate till failure. It is worth noting that the ASTM standard loading nose diameter is 0.25 inches. The support length was 0.59 inches. All SB specimens failed in tension in the middle of the specimen as shown in Figure 2. The average failure load value was 209 N (47 lbs), which was too low to introduce any compressive damage under the loading nose or near the lower support locations.

All coupons exhibited similar behavior. Figure 3 shows typical Lagrange surface strain tensor components measured right before failure using the digital image correlation (DIC) technique for full-field measurement of surface deformation. The reader is referred to [14] for a general description of the DIC technique, and to [11] for more specific details pertinent to this work. In addition, it is worth noting that the strain contour plots in Figure 3 were generated with the VIC-3D software [14]. The DIC strain analysis used a subset (data point) size of 31×31 pixels, corresponding to approximately 0.227 mm² for these particular tests. Data were obtained on 7 pixel centers, resulting in approximately 6,000 data points per load case.

The strain distributions in Figure 3 are well within the linear elastic range [11]. Also the SB coupons exhibit linear through-the-thickness axial strain ϵ_{33} distribution throughout the coupons, including the cross section corresponding to the failure location. Such observations can be used to derive simple closed-form approximations for the maximum axial normal stress in the SB coupon [11]

$$(1) \quad \sigma_{33} = \frac{MH}{2I}, \quad M = \frac{PL}{4}, \quad I = \frac{WH^3}{12}$$

where P is the applied force, L is the support length, and H and W denote the thickness and width.

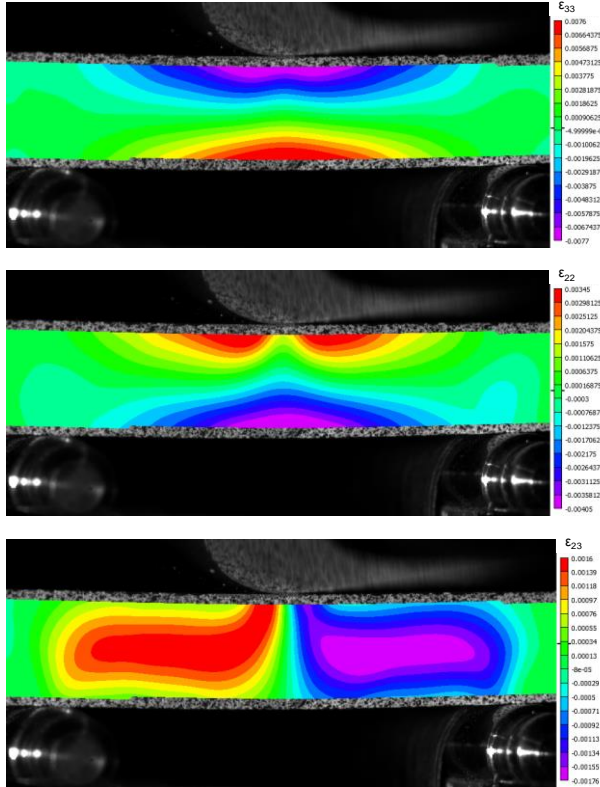


Figure 3. Lagrange surface strain tensor components measured right before delamination failure.

Equations (1) applied to the SB coupons tested in this work yield a 115.1 MPa (16.7 Ksi) (COV 3%) approximation for the ILT strength.

To verify the accuracy of the closed-form ILT stress approximation, a linear three-dimensional finite element model was built in the ABAQUS commercial finite element analysis code [15]. The average failure load value, the short-beam specimen dimensions as well as the attachment locations and sizes are listed earlier in this Section. The finite element model accurately simulated the loading nose and the supports including contact [11, 13]. The following material constitutive properties were utilized [13]: $E_{11} = 157$ GPa (22.7 msi); $E_{22} = E_{33} = 8.96$ GPa (1.3 msi); $\nu_{12} = \nu_{13} = 0.32$; $\nu_{23} = 0.5$; $G_{12} = G_{13} = 5.08$ GPa (0.737 msi); and $G_{23} = 2.99$ GPa (0.433 msi). The reader is referred to [13] for the details of the finite element mesh. The finite element analysis resulted in a 116.5 MPa (16.9 ksi) interlaminar tensile strength value which was similar to the 115.1 MPa (16.7 ksi) closed-form approximation (1).

3. COMPARISON WITH CURVED-BEAM TEST RESULTS

Ten 36-ply thick IM7/8552 unidirectional CB coupons were manufactured and tested to compare the ILT strength with the short-beam tests results. The CB coupons were manufactured per ASTM D 6415 specifications [6], except the width was reduced from 25.4 mm (1 in) to 12.7 mm (0.5 in). A 6.6 mm (0.26 in) flat flange thickness corresponds to 0.183 mm (0.0072 in) cured-ply thickness similar to the SB coupons. The average cured ply thickness in the radius of the CB specimens was up to 5% higher compared to the flat flanges. A CB laminate was laid on a male tool (an angle bracket), and a matching female tool (another angle-bracket) was placed on top of the laminate and cured in an autoclave. The outer corner of the male bracket had approximately 6.4 mm (0.25 in) radius and the inner corner of the female bracket had approximately 12.7 mm (0.5 in) radius. These two brackets formed the inner and outer surfaces and corners of the curved-beam laminate. After the laminate was cured, it was cut into curved-beam coupons. Figure 1 shows the ASTM D6415 test setup and tensile delamination failure. All static specimens were tested at the standard 0.05 in/min displacement rate, and exhibited similar behavior.

It is worth noting that the CB specimens used in this work are 0.5-inch wide although the ASTM D 6415 recommends 1-inch width. The width has been reduced based upon previous tests of both 1-inch and 0.5-inch wide CB specimens which resulted in similar interlaminar strength values as well as scatter. Specifically, the most recent batch of six 1-inch wide and 0.26-inch thick unidirectional IM7/8552 CB tests conducted by the authors resulted in an average ASTM D 6415 ILT strength of 77.2 MPa (11.2 ksi) and a 21.4% COV which are close to the 72.5 MPa (10.5 ksi) ILT strength and the 26.5% COV resulting from the 0.5-inch wide CB specimens of the same thickness, tested in this work.

The average 72.5 MPa (10.5 ksi) ASTM D 6415 CB strength value is significantly lower compared to the 116.5 MPa (16.9 ksi) value generated based on the SB tests. Also, the 26.5% COV in the CB strength is more than eight times higher compared to the 3% COV in the ILT strength reported from the SB tests.

4. REFINEMENT OF THE CURVED-BEAM METHOD TO ACCOUNT FOR POROSITY

ASTM Standard D 6415 underscores the sensitivity of measured ILT strength to void content. Consequently, the test results may reflect manufacturing quality as much as material properties [6]. An industrial computed tomography (CT) system with a 225 KV Microfocus X-ray tube and Varian 4030E series flat panel detector, built by North Star Imaging, Inc. was utilized in this work to detect porosity in the CB test

specimens. The micro-CT scans were accomplished at 40 kV tube voltage and 400 μ A target current at 0.5 frames per second and 10.5x magnification resulting in 0.5×10^{-3} in (12 μ m) scan resolution. The dashed lines in Figure 1 outline the area of the CT scan. Specimen cross-sectional images were obtained from the 3D volumetric model reconstructed in the efX-CT software by North Star Imaging. About 1,000 through-the-width section images, approximately 1200x1600 pixels in size, were used for the void detection in each specimen. Void identification, classification and measurement were performed by the Numerical Technology Company software. The software applied binary threshold transformation based on the pixel intensity found at the local minimum between air and material peaks on the pixel histogram (representing the number of pixels at given intensity) for the full scan volume; and then used object labeling and elliptical shape fitting for void measurements and calculation of the porosity volume. The CT based measurements were conducted on all ten 0.5-inch wide specimens.

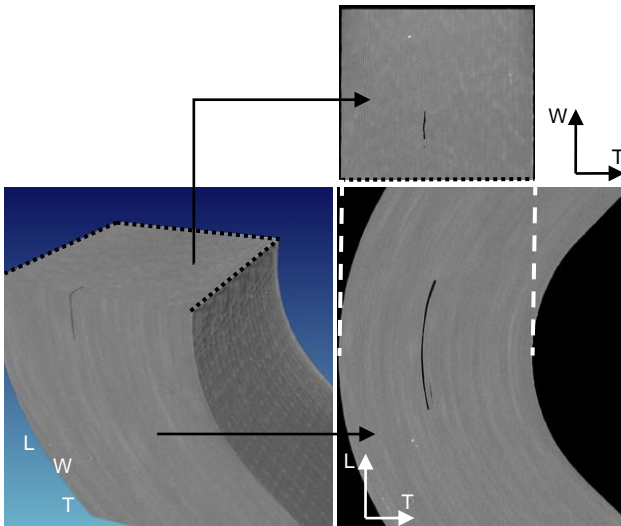


Figure 4. Void geometry in CB specimen 6.

Figure 4 shows examples of voids found in the CB specimens. Voids typically have the largest aspect ratios in the fiber direction resulting in thin curved shapes along the composite plies, and often degenerating into noodle-like shapes. Void thickness was found to be the smallest void dimension in all specimens. This defect geometry can be attributed to expansion of the air pockets that exhibit the largest resistance in the thickness direction due to curing pressure. It is worth noting that the porosity content in the CB specimens was low, e.g. the porosity content in the laminate thickness-based $0.26 \times 0.26 \times 0.26$ in³ ($6.6 \times 6.6 \times 6.6$ mm³) cube volumes throughout the CT scans in the CB radius area was less than 0.12%. However, it is not the porosity volume but the presence of the individual voids at the critical locations

in the CB specimens that reduce failure loads and causes large scatter.

The porosity volume alone is not sufficient for describing the effects or severity of voids. Indeed, a single large void located close to the mid-plane in the CB radius area is worse than a few dispersed smaller voids that add up to the same total volume. Reference [16] indicates that the porosity volume often does not correlate well with the degradation in structural performance.

Post-failure CT scans of the CB specimens confirmed that delamination passes through longer voids located around the mid-section of the specimens. Figure 5 shows typical cracks in the failed specimens. For all specimens, critical voids were identified in the CT scans before specimen failure and confirmed as the origin of the delamination crack in the corresponding post-failure CT scans. Critical voids are located in the vicinity of the maximum interlaminar tensile stress (about two third of the thickness in the middle of the radius area). Table 1 lists the geometry and reference locations of the critical voids.

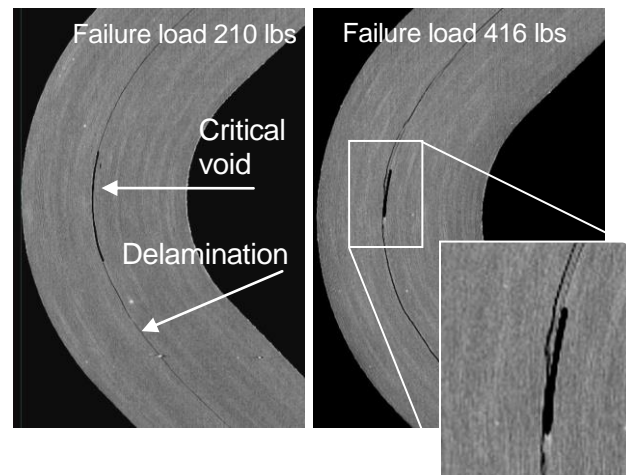


Figure 5. Examples of CT slices showing sections of CB specimens 6 (left) and 7 (right) after failure.

Figure 6 shows the trend in the failure load reduction as a function of the void area. The failure loads were normalized by 3.21 KN (722 lbs) corresponding to the failure load of a CB specimen without porosity. To calculate the failure load in the pristine CB coupon, a 116.5 MPa (16.9 ksi) ILT strength value was used based on the SB tests. Data suggests that the failure load decreases proportionally to the negative power of the void area. A 0.01 in² (6.45 mm²) void located in the critical area results in almost 60% reduction in the failure load according to this trend. It is worth noting that the locations of the critical voids in the radius area of CB specimens vary in the thickness and hoop directions. As the interlaminar tensile stress distribution in a CB coupon is non-uniform, the location of the critical void has an impact on the failure

load and explains the scatter in the data presented in Figure 6.

Table 1. Geometry and locations of critical voids in the CB specimen radius area. The radial location is measured from the outer radius, and the hoop location is measured from the apex of the curved part of the specimen.

Spec	Void Length mm (mil)	Width, mm (mil)	Thickness mm (mil)	Radial loc., % thickness	Hoop loc., degrees
1	1.5 (57)	0.7 (28)	0.14 (5.4)	86	0.2
2	4.8 (190)	1.3 (49)	0.19 (7.4)	78	39
3	1.4 (56)	0.5 (18)	0.23 (9.0)	53	26
4	0.7 (28)	0.5 (18)	0.19 (7.4)	40	-16
5	2.6 (100)	1.2 (47)	0.19 (7.4)	43	-1.3
6	5.6 (220)	2.4 (94)	0.19 (7.4)	43	2.9
7	1.7 (68)	0.7 (28)	0.19 (7.4)	41	-5
8	0.21 (8.1)	0.3 (12)	0.07 (2.9)	52	2.3
9	0.27 (11)	0.17 (6.8)	0.05 (1.9)	57	18
10	0.6 (25)	0.22 (8.7)	0.03 (1.3)	72	-5.5
Avg	1.9 (76)	0.8 (31)	0.15 (5.8)	57	6.1

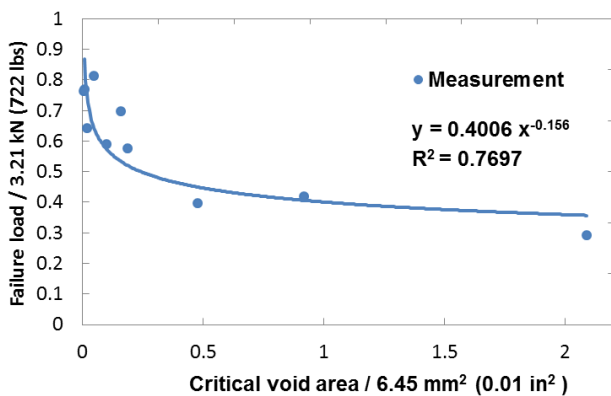


Figure 6. Dependency of CB failure load on the area of the critical void.

The combined effects of the void geometry and location are captured by the FE analysis of the stress concentration near the critical void under the known applied failure load. CT measurements are transferred into FEM by using ABAQUS scripting capability [15] to automatically build a structured three-dimensional local mesh of the volume around the critical void. Voids are represented by a tri-axial ellipsoid defined by the thickness and two aspect ratios in the fiber and width directions as shown in Figure 7. Linear 8-noded hexagonal 3D elements with reduced integration scheme (C3D8R) were used in the model. A typical total number of degrees of

freedom (DOF) is in the 500K-800K range. Mesh refinements are defined around the void and convergence of local stresses was verified. Displacements from the global model of the curved-beam specimen at failure load are applied as boundary conditions for the six faces of the local model volume. An FE mesh for the global model is illustrated in Figure 7 and includes a total of 560K DOF using the C3D8R hexagonal elements. Frictionless contact was prescribed between the specimen and the support rollers modeled as analytical rigid surfaces. The non-linearity associated with large displacements was included.

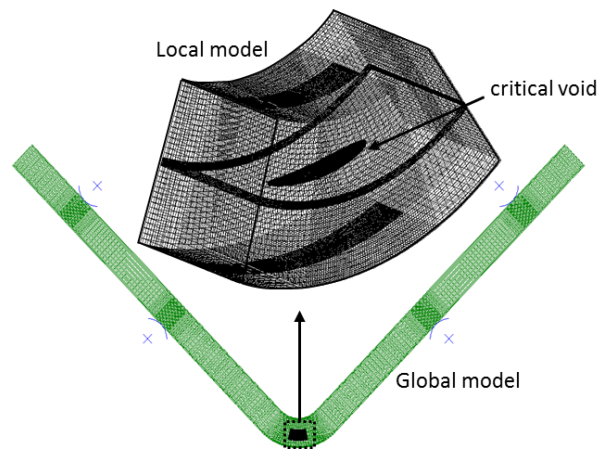


Figure 7. 3D structured FE mesh examples for a global model of the CB coupon and the local sub-model.

Figure 8 demonstrates that ILT stress concentration develops at the edge of the void along the longest dimension. The maximum stress concentration is typically found at surface locations corresponding to about mid-length of the void. Analysis of CT scans confirms that delamination initiates at this location as shown in the zoomed-in area in Figure 5. It is worth noting that while the local FE analysis approximated the voids as tri-axial ellipsoids in order to obtain converged mesh-independent stresses, the actual void shape varied, especially in the length-width plane. However, CT scans have shown that in most of the cases delaminations start close to the maximum width location as shown in Figure 5 (right). Interlaminar tensile and shear stress concentrations are spatially out of phase, with maximum shear stress concentration found at the void tip as illustrated in Figure 8.

Stress analysis results in all local models also demonstrated that the maximum interlaminar shear stresses at the void surface were much lower than the maximum interlaminar tensile stresses. As a consequence, the failure mode can be identified as tensile delamination. Interlaminar tensile stress concentrations at the critical void surfaces can be

extremely high. Numerical results for typical void geometries include concentration factors ranging between 8 and 20, which is consistent with the closed-form solutions provided in Reference [17] for a tri-axial ellipsoidal cavity in an infinite isotropic elastic body. However, the stresses quickly decay with the distance from the void as shown in Figure 9. The interlaminar tensile stress value at 100 μm (0.004 in) away from the critical location at the void surface in the radial direction is only 14% of the void surface stress.

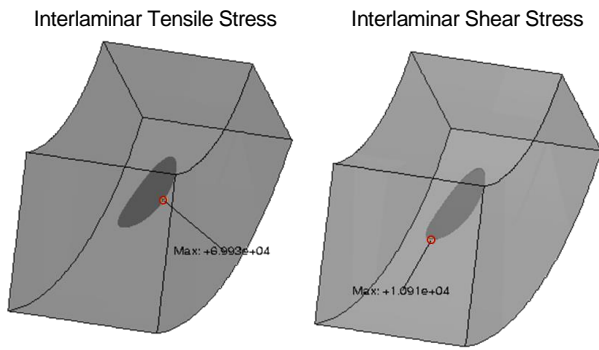


Figure 8. Locations of the maximum ILT stress (left) and the maximum shear stress (right) at the surface of the critical void.

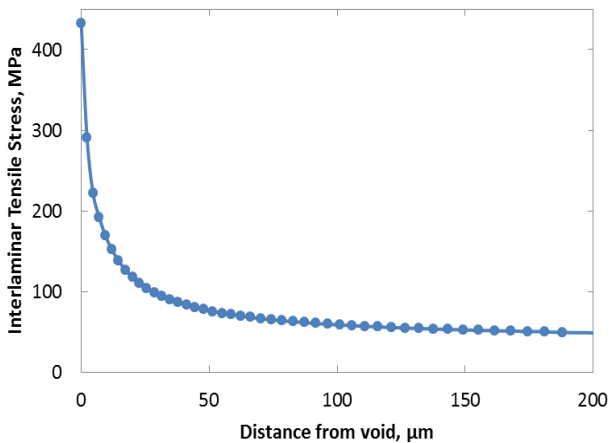


Figure 9. ILT stress versus the radial distance from the void surface.

The failure prediction in the presence of large stress gradients require investigation of stresses (or spatially averaged stresses) at a characteristic distance that could represent some gage length related to failure. The concept of using a characteristic distance to determine failure of composites in the presence of stress concentrations has been proposed in Reference [18]. The same work introduced the point-stress and average-stress failure criteria, where failure is determined by stresses at a finite characteristic distance or stresses averaged over a characteristic distance in the stress concentration region. These methods were applied to the stress concentrations at the critical voids, calculated by the FE analysis of the

curved-beam specimens at their failure loads. Point-stress and average-stress failure predictions typically rely on the calibration of the characteristic distance. In the current proposed methodology, no calibration or a-priori knowledge of characteristic distances is required. Instead, in the point-stress method, the local interlaminar stresses were plotted for each specimen as a function of the distance from the void; and in the average-stress method, the spatial average of the interlaminar tensile stress was considered. At each distance, the COV of the point-stress and the average-stress data were also plotted. By examining the COV dependence on the distance from the void, a unique and distinctive minimum point was identified as illustrated in Figure 10 for the point-stress and average-stress methods. The distance corresponding to the minimum COV can be considered as the optimal characteristic distance; and that distance was used to determine the refined interlaminar tensile strength value. A characteristic distance of 19 μm (7.3×10^{-4} in) was reported for the point-stress method and 89 μm (3.5×10^{-3} in) for the average-stress method.

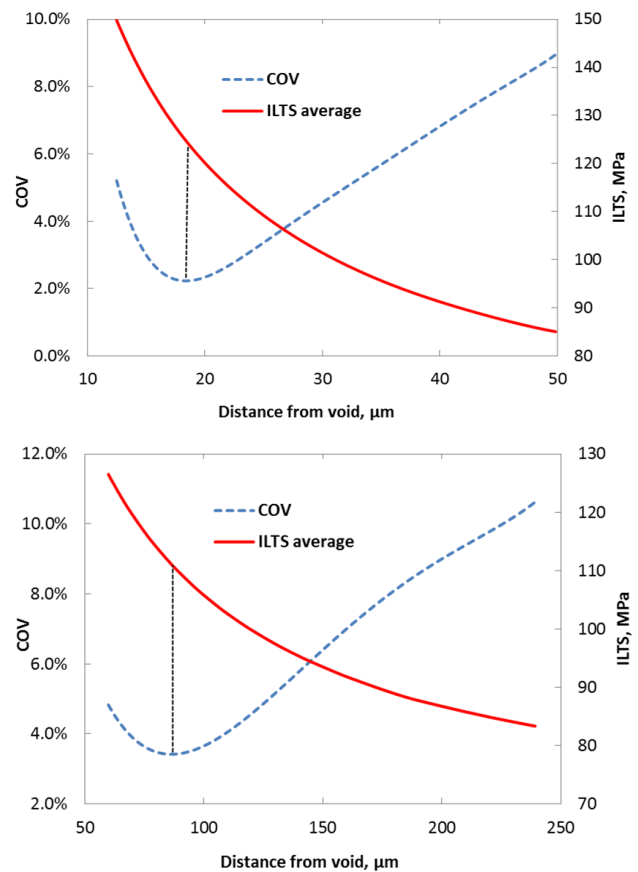


Figure 10. Characteristic distance and the interlaminar tensile strength (ILTS) using the point-stress (top) and the average-stress (bottom) method.

The average ILT strength values are 124.3 MPa (18.0 ksi) for the point-stress method and 110.4 MPa (16.0

ksi) for the average-stress method. Results for the ten curved-beam specimens are summarized in Table 2 and compared to the stresses calculated using ASTM D 6415 [6]. The average interlaminar tensile strength values found using the refined CB test methodology agree with the 116.5 MPa (16.9 ksi) ILT from the SB tests. Note that COV in the point-stress and the average-stress based ILT strength calculations are only 2.1% and 3.2% compared to 26.5% COV in the ASTM D 6415 approximation. Low scatter suggests that the refined ILT strength is appropriate as a pristine (free of defects) material property. And the CB test is useful for assessing the effects of porosity on ILT strength.

Table 2. Failure load, ASTM D 6415 and refined interlaminar tensile strength (ILTS) for CB specimens with porosity defects.

Spec	Failure Load, kN (lbs)	ASTM D 6415 ILTS, MPa (ksi)	Refined ILTS, point-stress method, MPa (ksi)	Refined ILTS, average-stress method, MPa (ksi)
1	2.24 (503)	83.4 (12.1)	123.1 (17.9)	115.1 (16.7)
2	1.34 (302)	52.3 (7.6)	125.1 (18.1)	109.3 (15.8)
3	1.89 (425)	70.3 (10.2)	125.8 (18.2)	105.7 (15.3)
4	2.61 (586)	92.8 (13.5)	123.8 (18.0)	109.1 (15.8)
5	1.27 (286)	50.0 (7.3)	119.0 (17.3)	103.3 (15.0)
6	0.93 (210)	37.7 (5.5)	125.2 (18.2)	112.9 (16.4)
7	1.85 (416)	68.8 (10.0)	129.3 (18.7)	112.0 (16.2)
8	2.47 (555)	94.6 (13.7)	125.8 (18.2)	113.0 (16.4)
9	2.45 (550)	93.9 (13.6)	123.9 (18.0)	109.3 (15.9)
10	2.06 (463)	81.5 (11.8)	121.5 (17.6)	113.8 (16.5)
Avg	1.91 (430)	72.5 (10.5)	124.3 (18.0)	110.4 (16.0)
COV	28.2%	26.5%	2.1%	3.2%

5. EFFECTS OF DEFECTS ON THE ILT FATIGUE PERFORMANCE

This Section presents *S-N* curves determined based on fatigue testing of CB coupons. Twenty 36-ply thick and 0.5-in wide IM7/8552 unidirectional curved-beam specimens were tested in fatigue. The ASTM D 6415 test fixture was placed in a uniaxial servo-hydraulic load frame with 25kN (5.5 kip) load cell capacity, and subjected to cyclic loads at 0.1 load ratio and 5 Hz frequency, to delamination failure. Figure 11 shows examples of fatigue delaminations in CB specimens after fatigue tests. The fatigue delaminations initiated in the radius area of the curved-beam specimens; and quickly propagated through the flanges. It is worth noting that the locations of the delaminations were not uniform among the specimens; and did not

necessarily coincide with the location of the maximum ILT stress in the porosity-free specimen. Secondary delaminations as well as delamination branching were observed in some of the curved-beam coupons.

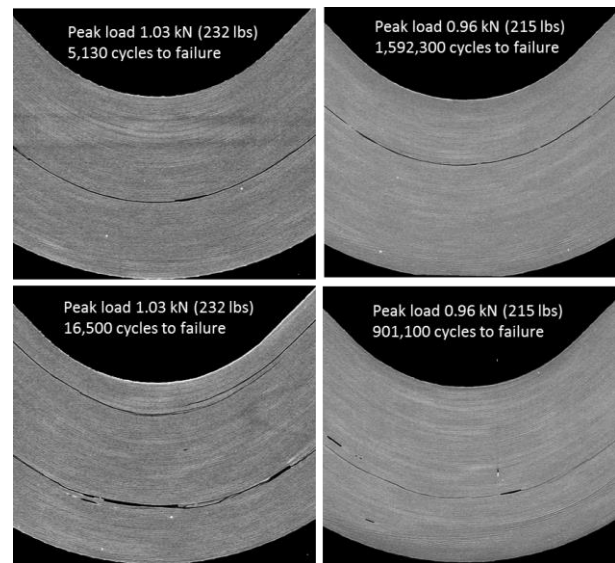


Figure 11. Examples of delaminations in IM7/8552 curved-beam fatigue test specimens.

The ILT peak stresses during fatigue testing were first calculated from a closed-form geometric ILT stress approximation listed in ASTM D 6415 [6]. The deformed shape of each specimen, used in the stress calculation [6] was obtained from initial monotonic loading up to the peak fatigue load value prior to the fatigue testing. The ILT *S-N* curve was generated by plotting the ratio of the interlaminar tensile peak stress and the interlaminar tensile strength against the log of the number of cycles to failure. The 72.5 MPa (10.5 ksi) static ILT strength was generated based on the 10 ASTM D 6415 CB tests.

The interlaminar tensile *S-N* curve and the least-squares fit for the power-law are illustrated in Figure 12. A large scatter with a low R^2 value of 0.337 is reported. Such a poor correlation cannot support reliable assessment of ILT fatigue material properties based on the ASTM D 6415 ILT stress approximation that assumes homogeneous (defect-free) anisotropic material in the CB test specimens [6 – 8].

Post-failure CT scans showed that the delamination crack typically passes through the longer voids located in the radius area of the CB specimens. In particular, the presence of larger individual critical voids explained that in several specimens the delamination crack was located relatively far away from the theoretical radial location of maximal interlaminar tensile stress (about 2/3 of the thickness). The presence of larger voids on the delamination path is illustrated in Figure 11. Porosity content in the CB fatigue specimens was low, e.g. the porosity content in

the laminate thickness-based $0.26 \times 0.26 \times 0.26 \text{ in}^3$ ($6.6 \times 6.6 \times 6.6 \text{ mm}^3$) cube volumes throughout the CT scans in the curved-beam radius area was less than 0.12%. Therefore, it is not the porosity volume but the presence of individual voids at critical locations that might cause the large scatter in the fatigue results presented in Figure 12. The effects of critical voids on the ILT stresses must be included for potential improvement of the fatigue characterization.

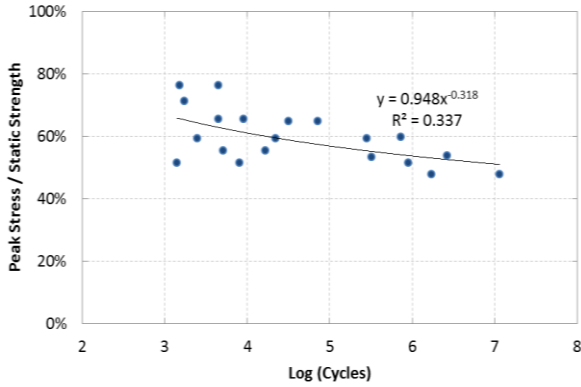


Figure 12. ILT S-N curve for IM7/8552 tape based on the ASTM D 6415 stress approximation.

The methodology presented in the Section 4 was applied to refine the ILT S-N curve based on the fatigue tests of the CB specimens, micro-CT measurement of porosity in the radius area, and the refined stress calculation that accounted for the porosity defects. Point-stress and average-stress based characteristic distances determined from the static curved-beam tests were used to determine the peak fatigue ILT stresses at critical voids and replace the closed-form ASTM D 6415 ILT stress approximation. For each of the 20 curved-beam fatigue coupons tested, critical voids were detected from CT scans using the measurement methods described in the Section 4, and the measurements were transferred into local FE sub-models. Displacement boundary conditions in the local FE models were generated from the global FE models of the curved-beam specimens subject to the peak fatigue loads. For the point-stress method, the defect-free peak stresses were determined by calculating the ILT stresses at the $19 \mu\text{m}$ ($7.3 \times 10^{-4} \text{ in}$) characteristic distance from the void's surface, as defined in the Section 4. In the average-stress method, the ILT stresses were averaged over the $89 \mu\text{m}$ ($3.5 \times 10^{-3} \text{ in}$) characteristic distance also defined in the previous Section. The ILT stresses at the peak fatigue loads were normalized by the corresponding ILT strength; and plotted against the log of the number of cycles to failure to generate the ILT S-N curves. The ILT strength values based on the point-stress and the average-stress methods are listed in the Section 4.

The ILT S-N curves from both methods are presented in Figure 13. Both S-N curves are similar, with less than 2% relative difference in the exponent. The refined exponent more than doubles the exponent of the fatigue curve based on the ASTM D 6415 ILT stress approximation. A $0.92 R^2$ value corresponding to the point-stress method and $R^2=0.94$ to the average-stress method are much stronger compared to the $R^2=0.34$ from the ASTM D 6415 ILT stress approximation. The more consistent S-N curves correspond to a pristine (porosity-free) material structure. The reduced scatter supports the ability of the refined ILT stress analysis methods to capture the effects of porosity on fatigue performance.

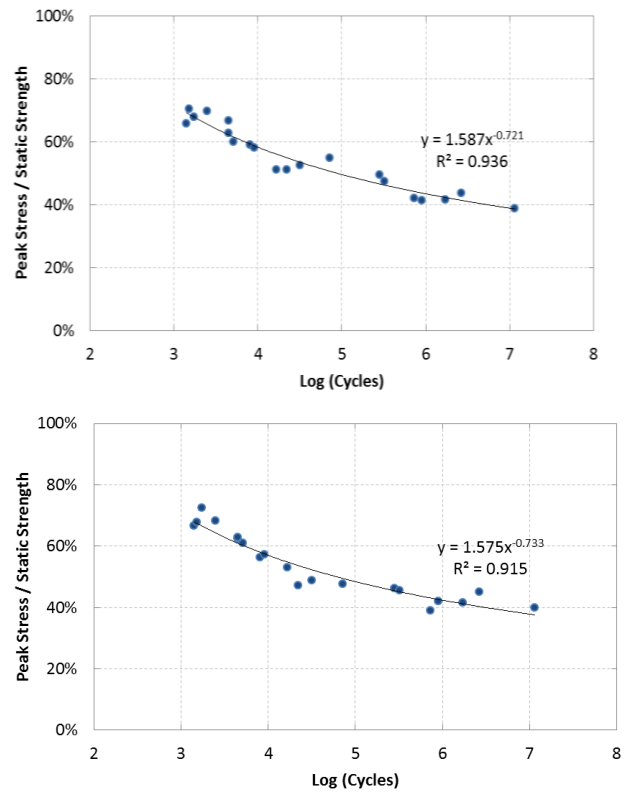


Figure 13. ILT S-N curves refined by the point-stress method (top curve) and the average-stress method (bottom curve.)

6. CONCLUSIONS

This work introduced the rotorcraft engineering community to advanced structural methods that could account for manufacturing issues including porosity in composite parts and enable accurate assessment of their capability and useful life. Composite aircraft structures must undergo a fundamental shift from fleet statistics to accurate assessment of condition for individual parts in order to enable both safe and economical usage and maintenance. Technologies to measure defects and understand their effects on strength and fatigue performance could enable that shift. Our goal is to make such technologies the

industry standard practice in the existing aircrafts and the emerging composite aircraft platforms.

In this work, CT measurements of porosity defects present in CB composite test articles were integrated into finite element models to assess the effects of defects on the ILT strength and fatigue behavior. Once the effects of defects were captured through transfer of the CT measurements into a three-dimensional structural model, the scatter in the test data was reduced; and reliable material ILT strength and fatigue properties were determined.

This work presents a modification to the ASTM Standard D 6415 CB method. The current ASTM D 6415 significantly underestimates the ILT strength as the CB coupon test data are affected by porosity even at a low content. The refinement to the ASTM D 6415 includes measurement of the critical voids in the CB radius area and transition of the defect information into a finite element stress analysis model to capture the ILT material strength properties. The ILT strength results of the modified CB tests presented for the IM7/8552 carbon/epoxy tape composite, popular in rotorcraft applications, are in excellent agreement with the SB based verification tests.

The methodology to determine the ILT material properties was further extended to characterizing the fatigue behavior. As an example, the ILT *S-N* curve corresponding to a 0.1 load ratio was determined for the IM7/8552 tape composite system.

The methodology presented in this work could become a standard practice for assessing the effects of porosity on the ILT strength and fatigue behavior. Indeed, porosity can be easily introduced in the CB specimens; and the susceptibility of the CB radius area to delamination limits the nondestructive inspections to the radius area and makes such specimens good candidates to study the effects of porosity on material strength. Although scatter in the ILT strength is an inherent attribute of the CB specimens, the subject of curved-beam testing and analysis has a significant practical value to understanding the effects of porosity, and should be considered. Porosity in laminated composites is a common structural design problem, and the rotorcraft industry has been using curved-beam articles to investigate porosity. This work shows that it is not the porosity content but the presence of individual voids at critical locations that reduce the ILT strength and causes scatter in the strength and fatigue behavior. The refined CB methodology provides a practical means for defect-tolerant design applications, and it is applicable to various structural configurations.

The potential benefits of the ability to accurately measure the material structure and transfer such non-destructive measurement into structural failure models go well beyond the CB tests. This work shows that fidelity of the non-destructive inspection needed to

quantify the smallest voids, that would impact structural performance, becomes extremely important. Once knowledge of the part condition in terms of critical defect location and size, and their influence on residual strength and useful life are established, the ultimate goal of achieving the fundamental shift from statistics-based to condition-based structural substantiation and disposition will be realized.

ACKNOWLEDGEMENTS

This work is sponsored by the US Office of Naval Research under a Grant Award N00014-11-1-0916 to the University of Texas Arlington. This support is gratefully acknowledged. The specimens used in this work were manufactured by Bell Helicopter Textron. The authors are grateful to Mr. Edward Lee, Principal Engineer, Manufacturing R&D in this regard, and wish to thank Mr. Brian Shonkwiler, Research Associate and Ms. Paige Carpentier, PhD student, University of Texas Arlington, for their assistance with running the tests.

COPYRIGHT STATEMENT

The authors confirm that they, and/or their company or organization, hold copyright on all of the original material included in this paper. The authors also confirm that they have obtained permission, from the copyright holder of any third party material included in this paper, to publish it as part of their paper. The authors confirm that they give permission, or have obtained permission from the copyright holder of this paper, for the publication and distribution of this paper as part of the ERF2013 proceedings or as individual offprints from the proceedings and for inclusion in a freely accessible web-based repository.

REFERENCES

- [1] Makeev, A. and Nikishkov, Y. 2011. Fatigue Life Assessment for Composite Structure, *ICAF 2011 Structural Integrity: Influence of Efficiency and Green Imperatives*, Komorowski, J. (Ed.), Springer: 119-135.
- [2] Nikishkov, Y., A. Makeev, and G. Seon. 2010. "Simulation of Damage in Composites based on Solid Finite Elements," *Journal of American Helicopter Society*, 55:042009.
- [3] Nikishkov, Y., A. Makeev, G. Seon. 2013. "Progressive Fatigue Damage Simulation Method for Composites," *International Journal of Fatigue*, 48:266-279.
- [4] US Department of Defense. Military handbook – MIL-HDBK-17-1F: Composite materials handbook, Polymer Matrix composites guidelines for characterization of structural materials; 2002: vol. 1.

- [5] Dobyns A., Rousseau C.Q., Minguet P. 2000. Helicopter applications and design. Delaware Composite Design Encyclopedia; 5:223-42.
- [6] American Society for Testing and Materials. 2006. Standard Test Method for Measuring the Curved Beam Strength of a Fiber-Reinforced Polymer-Matrix Composite. ASTM Standard D 6415/D 6415M, ASTM International.
- [7] Lekhnitskii, S. G. 1968. *Anisotropic Plates*, Gordon and Breach Publishers, New York, pp. 95-101.
- [8] Kedward, K. T., R. S. Wilson, and S. K. McLean. 1989. "The Flexure of Simply Curved Composite Shapes," *Composites*, 20(6):527–553.
- [9] Hexcel Corporation. 2013. HexPly 8552 Epoxy Matrix, Product Data, available online at http://www.hexcel.com/Resources/DataSheets/Prepreg-Data-Sheets/8552_us.pdf, last accessed on June 20, 2013.
- [10] American Society for Testing and Materials. 2007. Standard Test Method for Through-Thickness "Flatwise" Tensile Strength and Elastic Modulus of a Fiber-Reinforced Polymer Matrix Composite Material. ASTM Standard D 7291/D 7291M, ASTM International.
- [11] Makeev, A., Y. He, P. Carpentier, B. Shonkwiler. 2012. "A Method for Measurement of Multiple Constitutive Properties for Composite Materials," *Composites: Part A*, 43(12):2199–2210.
- [12] American Society for Testing and Materials. 2006. Standard Test Method for Short-Beam Strength of Polymer Matrix Composite Materials and Their Laminates. ASTM Standard D 2344/D 2344M, ASTM International.
- [13] He, Y., A. Makeev, and B. Shonkwiler. 2012. "Characterization of Nonlinear Shear Properties for Composite Materials Using Digital Image Correlation and Finite Element Analysis," *Composites Science and Technology*, 73:64–71.
- [14] Sutton, M. A., J.-J. Orteu, and H. W. Schreier. 2009. *Image Correlation for Shape, Motion and Deformation Measurements*, Springer.
- [15] ABAQUS 6.11.1 User's Manual. 2011. ABAQUS Inc, Pawtucket, RI, USA.
- [16] Lambert, J., A. R. Chambers, I. Sinclair, and S. M. Spearing. 2012. "3D Damage Characterization and the Role of Voids in the Fatigue of Wind Turbine Blade Materials," *Composites Science and Technology*, 72:337-343.
- [17] Chiang C.-R. 2008. "Stress Concentration Factors of a General Triaxial Ellipsoidal Cavity," *Fatigue and Fracture of Engineering Materials and Structures*, 31:1039-1046.
- [18] Whitney, J. M., and R. J. Nuismer. 1974. "Stress Fracture Criteria for Laminated Composites Containing Stress Concentrations," *Journal of Composite Materials*, 8:253-265.